aerospace

MDPI

Article

Effects of Gas Thermophysical Properties on the Full-Range Endwall Film Cooling of a Turbine Vane

Jian Liu, Mengyao Xu and Wenxiong Xi *

Research Institute of Aerospace Technology, Central South University, Changsha 410012, China; jian.liu@csu.edu.cn (J.L.); 15130715317@163.com (M.X.)
* Correspondence: 13739076081@163.com

Abstract: To protect turbine endwall from heat damage of hot exhaust gas, film cooling is the most significant method. The complex vortex structures on the endwall, such as the development of horseshoe vortices and transverse flow, affects cooling coverage on the endwall. In this study, the effects of gas thermophysical properties on full-range endwall film cooling of a turbine vane are investigated. Three kinds of gas thermophysical properties models are considered, i.e., the constant property gas model, ideal gas model, and real gas model, with six full-range endwall film cooling holes patterns based on different distribution principles. From the results, when gas thermophysical properties are considered, the coolant coverage in the pressure side (PS)-vane junction region is improved in Pattern B, Pattern D, Pattern E, and Pattern F, which are respectively designed based on the passage middle gap, limiting streamlines, heat transfer coefficients (HTCs), and four-holes pattern. Endwall η distribution is mainly determined by relative ratio of ejecting velocity and density of the hot gas and the coolant. For the cooling holes on the endwall with an injection angle of 30°, the density ratio is more dominant in determining the coolant coverage. At the injection angle of 45°, i.e., the slot region, the ejecting velocity is more dominant in determining the coolant coverage. When the ejecting velocity Is large enough from the slot, the coolant coverage on the downstream endwall region is also improved.

Keywords: endwall film cooling; thermophysical property; turbine vane; coolant coverage

check for updates

Citation: Liu, J.; Xu, M.; Xi, W. Effects of Gas Thermophysical Properties on the Full-Range Endwall Film Cooling of a Turbine Vane. *Aerospace* **2023**, *10*, 592. https://doi.org/10.3390/aerospace10070592

Academic Editor: Konstantinos Kontis

Received: 28 April 2023
Revised: 19 June 2023
Accepted: 27 June 2023
Published: 28 June 2023

1. Introduction

Film cooling is the most effective method to protect turbine blades from heat load damage by ejecting coolant flows from several discrete cooling holes. Film cooling can use compressed air within gas turbine systems, and reduce temperature on the solid surfaces directly and effectively, although it is associated with reduced aerodynamic efficiency. The benefits of film cooling are that it uses the compressed air and decreases the blade surface temperature directly [1].

The endwall film cooling of the first-stage vane is designed to safeguard the endwall from the thermal load originating from the combustor's exhaust gas. This cooling approach is challenging due to the complex flow characteristics, such as horseshoe vortices and passage vortices, which influence coolant coverage on the endwall [2], particularly concerning the first-stage vane. Prior research has largely concentrated on two difficult areas: the leading edge (LE) region and the vane-pressure side (PS) junction region, both of which are characterized by a strong transverse pressure gradient. Some film cooling results gathered from flat plates are not directly applicable [3,4]. Over recent decades, extensive research has been conducted on endwall film cooling in a linear or annular cascade [5–18]. Simon and colleagues [5,6] carried out film cooling measurements on a contoured endwall with a nozzle guide vane. The suction side (SS) coolant migration vanished and the mixing effect became more apparent at higher coolant flow rates. Meanwhile, Knost and Thole [8] gauged the film cooling effectiveness (η) on the endwall for the first-stage vane. Their observations highlighted two areas, namely the LE region and the PS-endwall junction region, where it was particularly challenging for coolant flows to achieve coverage. Ghosh and Goldstein [9] explored the impact of the inlet skew on heat and mass transfer within a linear cascade. Their findings indicated that the inlet skew had notable effects on the PS due to its interaction with the passage vortex. Shiau et al. [10,11] showcased comprehensive endwall effectiveness contours, employing combinations of layback fan-shaped and cylindrical holes arranged on the vane using a pressure-sensitive paint (PSP) technique in annular cascades. Their research corroborated that PSP is a promising method for measuring high-quality cooling effectiveness (η). In a separate study, Yang et al. [12] analyzed the conjugated heat transfer on the endwall, taking into account the effects of upstream purge flow. Their findings highlighted that the purge flow significantly enhanced the overall cooling effectiveness on the endwall, especially its uniformity. Chen et al. [13,14] studied full-coverage film cooling on a non-axisymmetric contoured endwall. They concluded that the contoured endwall outperformed the flat endwall. Bu et al. [16] established a turbine endwall with a combined regime of jet impingement and film cooling, and investigated four types of geometric parameters. They performed an Analysis of Variance (ANOVA) to scrutinize the primary effect of each parameter and the correlation between them.

Endwall film cooling is intricate due to the intense flow impingement and complex vortex structures. Despite extensive research on film cooling, the optimal configuration of cooling holes on the endwall remains unclear. As inferred from previous studies [19,20], the primary design principles for endwall film cooling are centered around pressure distributions. Liu et al. [21] explored the full-range endwall film cooling of a turbine vane, incorporating different design principles. The principles for the arrangement of cooling holes were based on pressure coefficients, streamlines, and heat transfer coefficient (HTC) distributions. Their findings suggested that designs premised on streamline distribution and HTC distributions result in greater coolant coverage, and the design based on HTC distributions could curtail high-temperature zones. In another study, Pu et al. [22] conducted an experimental investigation of overall cooling in laminated configurations at a turbine vane endwall. They discovered that a dense arrangement of large-diameter impingement holes was effective in enhancing the cooling efficiency of the pressure side corner.

However, most of the prior studies were conducted in low-temperature experimental setups or under simplified working conditions, often overlooking the effect of the thermophysical properties of gas. Recognizing the influence of the thermophysical properties of fluid, some foundational research has been undertaken. Zhang et al. [23] conducted a numerical investigation into liquid-film cooling under high pressure. Considering the gas in a two-phase liquid solution, the property of real gas, and varying thermophysical properties, they established a mathematical model for high-pressure film cooling. In another study, Nematollahi et al. [24] explored the evaluation of the cubic model of real gas in supersonic flow within a wedge-shaped cascade. They developed and compared four additional cubic model equations of real gas, based on the NIST Refprop model. However, they found that the Aungier-Redlich-Kwong equations of the state model provided superior accuracy. Yuan et al. [25] devised a new model for real gas to quantify and predict gas leakage in high-pressure gas pipelines. This model offers two significant enhancements: it employs the mass fraction to determine the proportion of leaked gas flow to in-pipe gas flow, and it incorporates real-gas thermodynamics into the fundamental governing equations.

In recent years, various studies focusing on the flow structures of high temperature and high-pressure gas within engine applications have considered the impact of realistic working conditions or real gas models [26–29]. Salvadori et al. [26] delved into the performance of high-pressure turbine endwall film cooling under realistic inlet conditions, such as non-uniformities of total temperature and velocity profile. They found that the inlet swirl restricts coolant coverage, as it alters the development of the horseshoe vortex (HV) and generates a stronger passage vortex (PV), which negatively affects platform cooling. Aiming to bolster cooling performance in the leading edge region, Wen et al. [27] examined the effects of leading edge film cooling arrangements via adiabatic and aero-thermal coupled simulation. Their research confirmed that the trenched configuration could be applied to the first-stage turbine vane to elevate inlet temperature and enhance engine efficiency. Bai et al. [29] probed into the effects of axisymmetric convergent contouring and blowing ratio on endwall film cooling and vane pressure side surface phantom cooling performance under real gas turbine operating conditions. Their findings suggested that the optimal endwall contouring shapes serve as an effective technical approach to reduce coolant depletion. Additionally, several fundamental research endeavors have been carried out to contemplate the effect of gas physical properties [23–25,30,31].

For cooling a turbine blade, lots of experiments have been performed in a low temperature test rig ignoring the variations of gas thermophysical properties. Considering the gas thermophysical properties, the blowing ratio and density ratio are changed in the real operation condition. For endwall film cooling, the interactions between different cooling holes are strong, so it is necessary to investigate the effect of gas thermophysical properties. Therefore, the effects of gas thermophysical properties on full-range endwall film cooling of a turbine vane are investigated in the present study. Six kinds of full-range endwall film cooling designs are considered with the validated turbulence model. Three kinds of gas thermophysical properties models are considered, i.e., the constant property gas model, real gas model, and ideal gas model. Flow structures and temperature fields of endwall film cooling are displayed and analyzed by three-dimensional numerical calculations.

2. Description of Computational Domain

For the simulation of endwall film cooling, a simplified guide vane is utilized, drawn from Knost's thesis [20] and magnified nine times from the original size. The computational domain is depicted in Figure 1, with relevant design and operational parameters outlined in Table 1. This domain comprises a main flow passage and a section for the coolant supply plenum. The main flow passage is constructed between two guide vanes, with an upstream extended part and a downstream extended part added to accommodate flow developments. The mainstream adopts a mass flow inlet with a rate of 1.6 kg/s and a Reynolds number of 128,600 (with dynamic viscosity selected at a temperature of 1700 K). The reference length corresponds to the vane's chord, which spans 594 mm. Results obtained under the same flow conditions as in Knost's work [20] serve as the benchmark for comparisons. Film cooling holes, angled at 30°, are distributed on the endwall. Coolant is supplied from a plenum, mirroring the real working conditions for endwall film cooling. In addition to the film cooling holes, a slot is located upstream of the holes, offering supplementary protection for the endwall. A similar slot is referenced [5,6], resulting from the assembly of two endwall components. Positioned 0.31C upstream of the vane are the slot aids in the coolant supply from the slot and the film cooling holes. Accordingly, two parameters, *S* and *F*, are defined to represent the coolant mass flow rate from the slot and the film cooling holes in relation to the mainstream flow rate.

Table 1. Related Geometric parameters and flow conditions.

Geometric Parameters		Flow Conditions	
Scale	9	Inlet Reynolds number	128,600
Span of the vane	S_p = 552.42 mm	Inlet mass flow rate	1.6 kg/s
Chord of the vane	C = 594 mm	S	1–2%
Pitch between adjacent vanes	P = 457.38 mm	F	1–2%
Coolant injection angle	α = 30°	Inlet mainstream turbulence intensity	8%

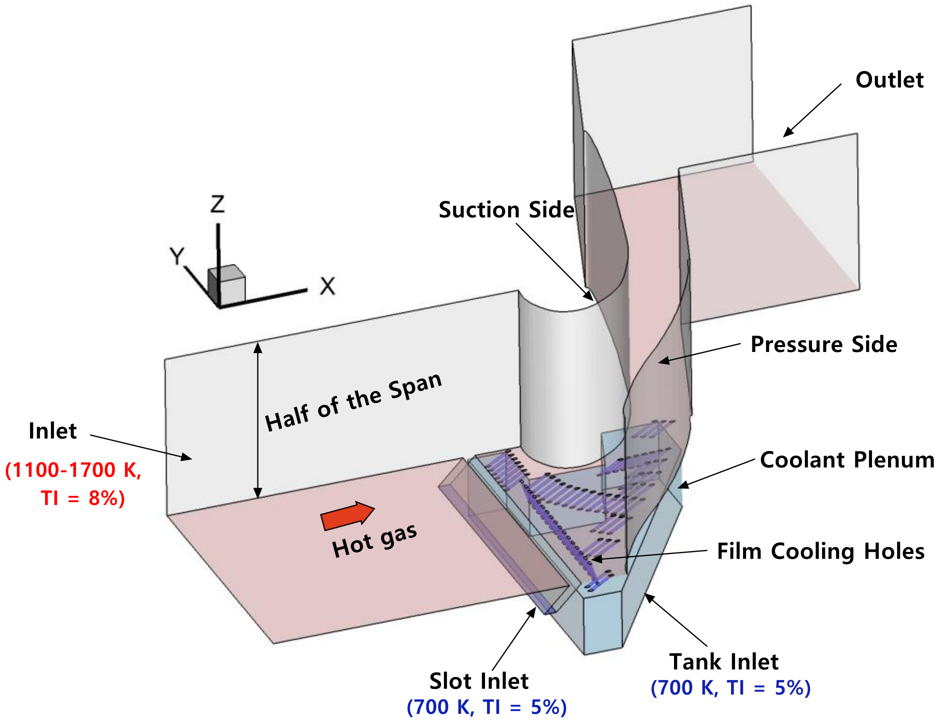

Figure 1. Schematic of the computational domain.

$$S = \frac{Slot\ mass\ flow\ rate}{Mainstream\ mass\ flow\ rate} \tag{1}$$

$$F = \frac{Film\ holes\ mass\ flow\ rate}{Mainstream\ mass\ flow\ rate} \tag{2}$$

In this paper, the S and F are set as 1–2%, respectively. The effects of mass flow rate ratio are considered.

The arrangement of endwall film cooling holes is based on varied principles, resulting in six different configurations, as shown in Figure 2. Pattern A and Pattern B have their roots in previous arrangements derived from references [20,32]. Pattern B, in particular, considers the effects of the slot that forms when two endwall components are assembled. Pattern C, Pattern D, and Pattern E are designed on the basis of pressure distributions, streamline distributions, and heat transfer coefficient distributions, respectively, with the aim of enhancing coolant coverage. These distributions are calculated without factoring in the impact of coolant flows from endwall film cooling holes. Pattern F, meanwhile, is also predicated on pressure coefficients and introduces a four-hole pattern. Leveraging the fractal theory, this four-hole pattern provides advantages in enhancing local coolant coverage. For Patterns A-E, film cooling holes are organized with a pitch ratio (P_c/D) of 3. For Pattern F, the distance separating two opposing film cooling holes is four times their diameter ($4D$). All film cooling holes are cylindrical with an injection angle of 30°, and are arranged on the endwall with a length ratio of 10. Regardless of the design, the mass flow rate remains constant, with the total number of cooling holes ranging between 40 and 50.

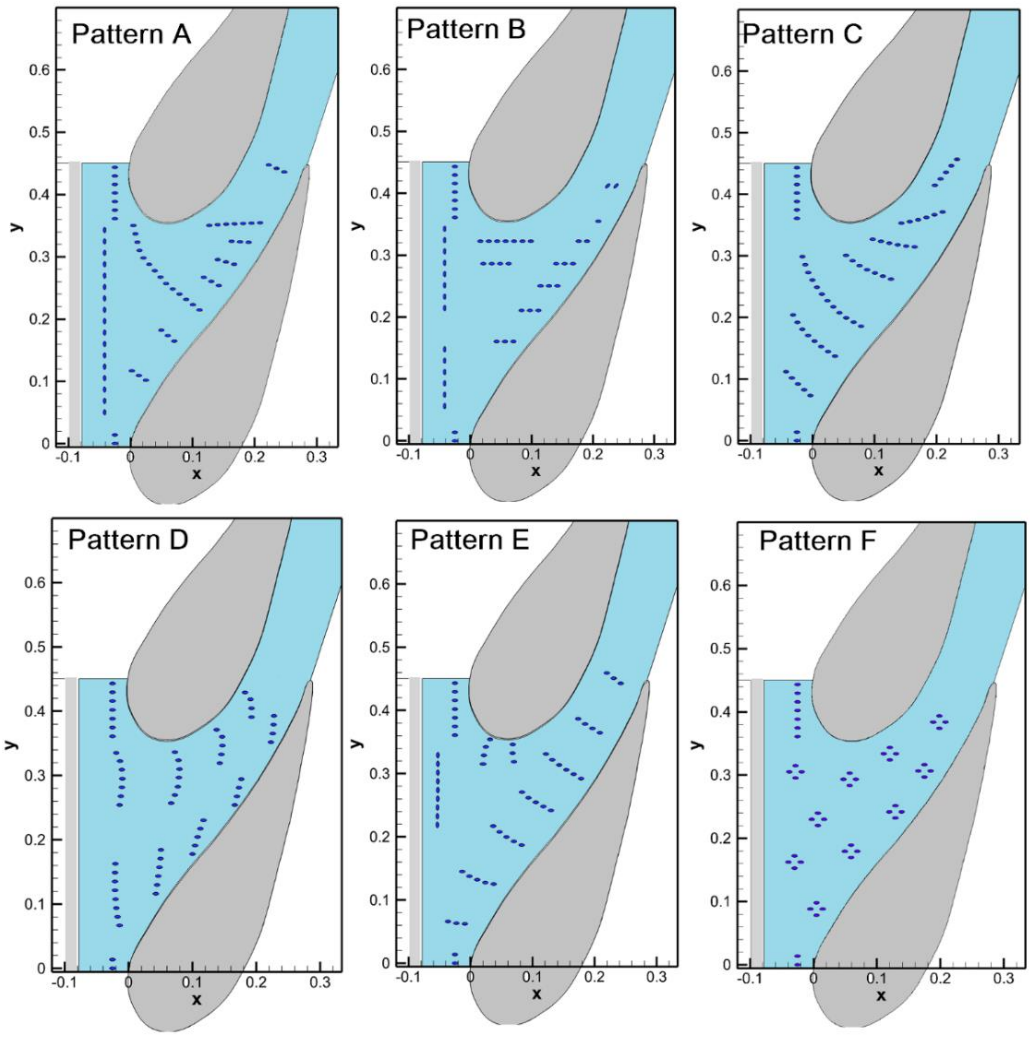

Figure 2. Different patterns of film cooling holes arranged on the turbine endwall.

3. Computational Method and Procedure

3.1. Mesh Details

This paper employed ANSYS Fluent 19.1 to generate the meshes, due to the complexity of the computational domain. The domain is divided into several sub-domains for the purpose of mesh generation, as detailed in Figure 3. These sub-domains are interconnected through interfaces which facilitate the transfer of result data. These interfaces ensure accurate data transfer between two distinct mesh surfaces through interpolation. Structured meshes are utilized within each sub-domain in an effort to decrease mesh quantity and enhance computational accuracy. Due to the employment of the k-ω SST turbulence model, meshes located near the walls are densely packed, with wall y plus approximately equal to one. For each sub-domain, unique mesh strategies such as O-block and Y-block are implemented to boost mesh quality. Furthermore, the region encompassing the interfaces also features exceptionally dense meshes, ensuring accurate and seamless data transfer.

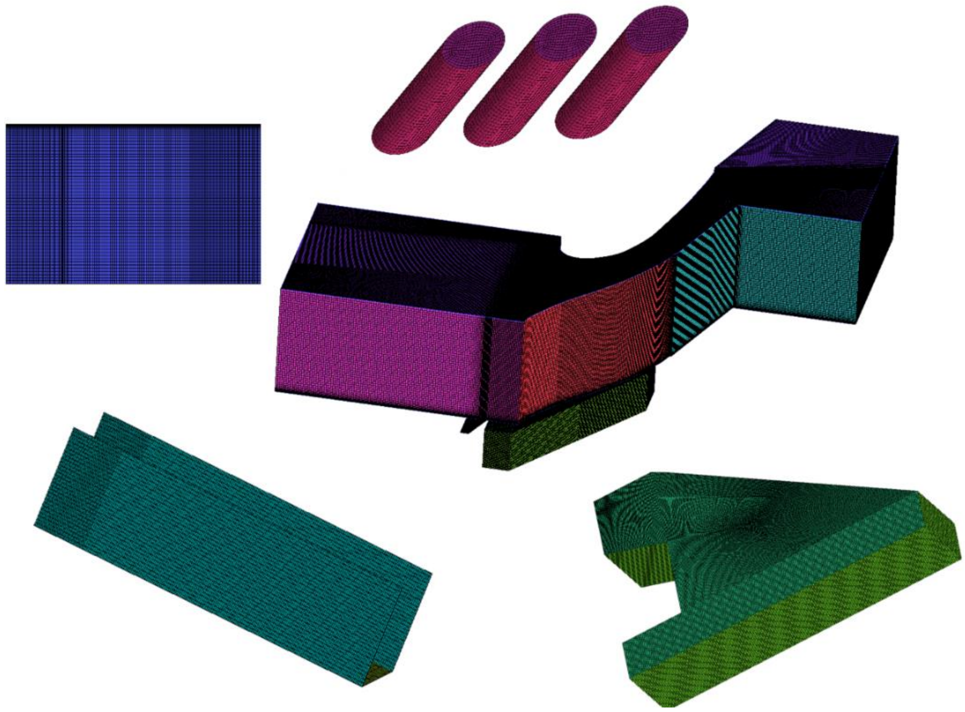

Figure 3. Overview of the generated structured meshes.

A mesh independence study is performed by Pattern D at film cooling mass flow ratio = 2% and slot mass flow ratio = 1%. Four kinds of mesh systems are designed with a grid number of 5.36 million, 7.63 million, 10.29 million, and 13.69 million, respectively. The mesh systems are built based on node increase factors of 0.8, 0.9, 1.0, and 1.1. The pressure drop between the inlet and the outlet, and averaged film cooling effectiveness are used for the comparisons shown in Table 2. The pressure drops and film cooling effectiveness are obtained by an area-averaged method. The definition of η is below.

$$\eta = \frac{T_w - T_g}{T_c - T_g} \tag{3}$$

where T_{w} is the wall temperature, T_{g} is the hot gas temperature, and T_{c} is the coolant temperature.

From the table, the pressure drops predicted by different mesh systems have pretty good agreement, and the difference is within 1%. For averaged film cooling effectiveness, the difference between two mesh systems is within 2%. Considering the requirements of wall treatment function, calculation accuracy and computational efforts, the mesh system with a grid number of 10.29 M is selected.

Table 2. Comparisons of averaged pressure drop and cooling effectiveness (Pattern D).

	Scale Factor	**Total Meshes**	**ΔP (Pa)**	**η_{avg}**
Mesh 1	0.8	5,344,239	361.4	0.327
Mesh 2	0.9	7,552,357	361.5	0.326
Mesh 3	1.0	10,281,718	361.5	0.323
Mesh 4	1.1	13,746,964	361.5	0.322

3.2. Turbulence Model

The selection of turbulence model is important when solving the complex flow problem. In this work, the *k*-ω SST model is selected to deal with wall bounded flows on the turbine endwall. The *k-ω* SST model combines the advantage of the *k-ω* and *k-ε* models, which exhibit good accuracy in the prediction of wall shear flows.

The comparison of the predicted results with the experimental data is shown in Figure 4. Besides the film cooling effectives, the basic vane parameter, i.e., pressure coefficients and endwall heat transfer have been validated in previous work [21], and the related experimental data is obtained from [33]. Figure 4a compares η contours predicted by the *k-ω* SST model with the experimental data captured by the IR camera. The film cooling holes on the endwall are arranged according to experimental Model 1 and Model 2 in [33]. From the figure, the η distribution contour has good agreement with the experimental data. The large errors are found in the vane-endwall connection regions where the IR camera has poor accuracy. A large quantity of coolant ejects from the upstream slot and pushes the coolant flows from endwall cooling holes to the suction side. For this pattern of film cooling holes, the coolant upstream the LE has difficulty being ejected out, and more coolant is more easily ejected from the downstream cooling holes where the ambient pressure is small. Figure 4b presents the comparison of lateral averaged η arranged in Model 1 and Model 2. Each data point in the figure is obtained by averaging a cluster of result data in the spanwise direction. Overall, the trend of averaged η along the streamwise direction predicted by the numerical calculation matches the experimental data well, and the error is within 10%. A larger error can be found in the upstream region, where the coolants are mainly ejected from the slot. In the simulation, the inlet boundary condition of the slot is the set uniform velocity, but it is difficult to achieve this in the experiment. The different ambient pressure causes the different ejection pattern, and a relatively large error in the peak value. Based on the results, the numerical results predicted by the *k-ω* SST model have provided enough accuracy and can be used in the lateral calculation.

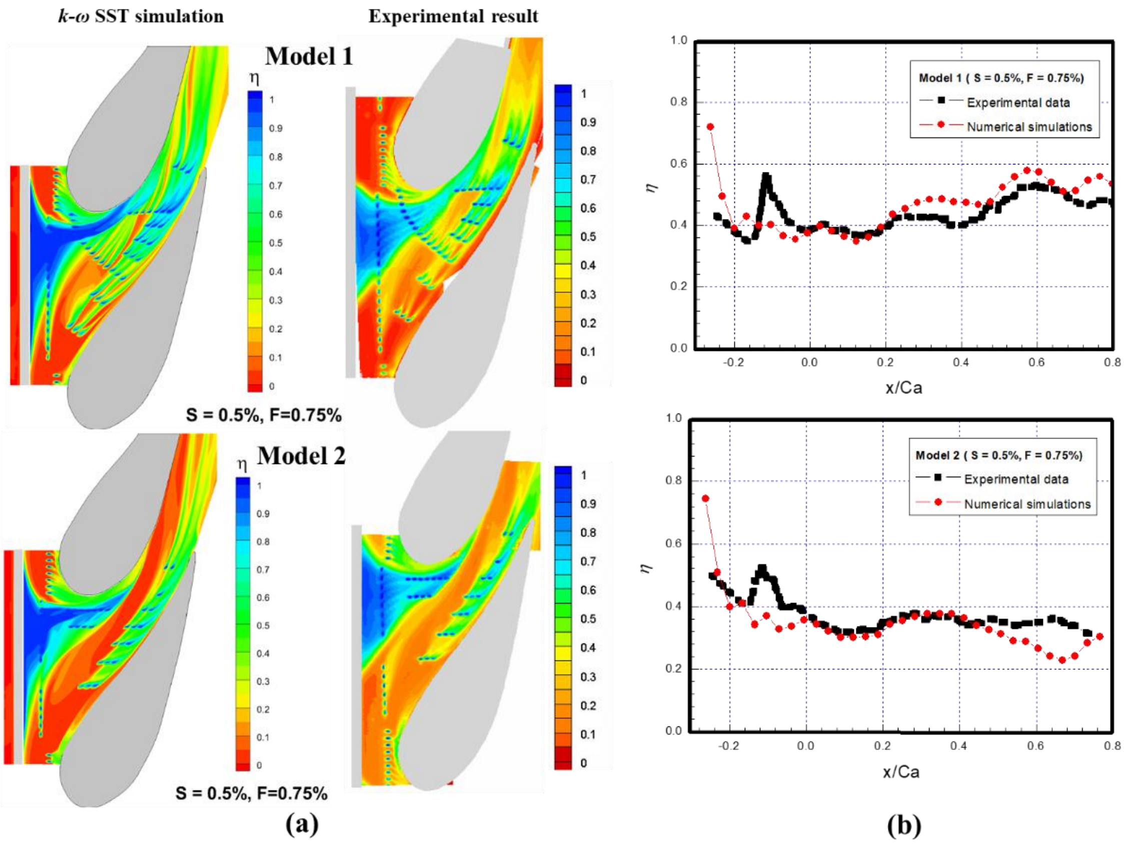

Figure 4. Validation of the turbulence model by comparing with the experimental data of Pattern A. (**a**) comparisons of the film cooling effectiveness contour. (**b**) comparison of lateral averaged film cooling effectiveness.

3.3. Gas Thermophysical Properties

The density of an ideal gas law in an incompressible flow is calculated by

$$\rho = \frac{P_{\mathrm{op}}}{\frac{R}{M_w} T} \tag{4}$$

where, R = the universal gas constant; M_{w} = the molecular weight of the gas; P_{op} = the operating pressure.

Ideal gas law is the simplest mathematical thermodynamic equation to connect temperature, pressure, and other items. However, it becomes increasingly inaccurate at higher pressures and lower temperatures. The Redlich-Kwong state equation [34] is improved to solve this problem, and the original form is

$$P = \frac{RT}{V - b} - \frac{\alpha_0}{V(V + b)T_r^{0.5}} \tag{5}$$

where P = absolute pressure (Pa); R = universal gas constant. V = specific molar volume ($\mathrm{m}^3/\mathrm{kmol}$); T = temperature (K); T_{r} = reduced temperature T/T_{c}; where T_{c} is the critical temperature; α_0 and b are constants related to the fluid critical pressure and temperature.

For the viscosity, Sutherland's law is used, and its form is below with three coefficients.

$$\mu = \mu_0 \left(\frac{T}{T_0}\right)^{3/2} \frac{T_0 + S}{T + S} \tag{6}$$

where μ = the viscosity in kg/m·s; T = the static temperature in K; μ_0 = reference value in kg/m·s; T_0 = reference temperature in K; S = an effective temperature in K (Sutherland constant). For air at moderate temperatures and pressures, μ_0 = 1.716 × 10^{-5} kg/m·s, T = 273.11 K and S = 110.56 K.

Thermal conductivity is obtained by kinetic theory.

$$k = \frac{15}{4} \frac{R}{M_w} \mu \left[\frac{4}{15} \frac{c_p M_w}{R} + \frac{1}{3} \right] \tag{7}$$

where R is the universal gas constant, M is the molecular weight, μ is the material's specified or computed viscosity, C_p is the material's specified or computed specific heat capacity.

Specific heat capacity is obtained by kinetic theory.

$$c_{p,j} = \frac{1}{2} \frac{R}{M_{w,j}} (f_i + 2) \tag{8}$$

where f_i is the number of degrees of freedom for the gas species.

For the constant gas properties, the thermophysical properties are obtained from Table 3 below. For the calculation case with constant gas properties, the gas properties are obtained by the temperature of the mainstream.

Table 3. Gas thermophysical properties at 1 Mpa from database of NIST.

Temperature (K)	**Density (kg/m^3)**	**Conductivity (10^{-2} W/m·K)**	**Capacity (kJ/kg·K)**	**Dynamic Viscosity (10^{-5} Pa·s)**
700	5.023	5.066	1.0781	3.33
1100	3.199	7.327	1.1631	4.44
1400	2.515	8.918	1.2154	5.17
1700	2.071	10.551	1.2677	5.85

3.4. Boundary Conditions and Solver

The boundary setting is the same with the experiments in Ref. [20]. The mainstream inlet is set as (1100–1700 K) with a turbulence intensity of 8%. The mass flow rate of the inlet is set as 1.6 kg/s, and corresponding Re is 128,600 when the inlet air is set at 1700 K (the dynamic viscosity is 5.85×10^{-5} Pa·s). The inlet region is built with an upstream extended channel to develop the inlet mainstream. In the calculation, three kinds of gas thermophysical properties models are applied in the solver, i.e., the constant property gas model, real gas model, and ideal gas model. For the constant property gas, the gas thermophysical model is determined by the mainstream. The corresponding thermophysical model is provided in Section 3.3. Half of the vane height is used in the computation domain to reduce the mesh quantity, and the symmetric boundary is set for the top wall. The periodic boundary condition is set for two sides, except the vane surfaces. The outlet is set as pressure outlet with an ambient pressure of 1 mPa. The coolant of the endwall film cooling holes is supplied by the plenum connected to the endwall, with a mass flow rate ratio of 1–2%. The temperature is set as 700 K, with a turbulence intensity of 5%. Mass flow inlet is chosen for the upstream slot, and flow mass rate ratio is set as 1–2% of the mainstream. The turbulence intensity setting in this work is based on an engine-like condition which is different from the experiment in Ref. [20].

The SIMPLEC method is employed to couple the pressure and velocity fields. The second upwind scheme is utilized for the discretization of pressure, momentum, turbulent kinetic energy, specific dissipation rate, and energy equations. The convergence is determined based on the residuals and average temperature on the endwall. Absolute criteria for continuity, x-velocity, y-velocity, z-velocity, k and ω items are set at 10^{-5}, and for the energy equation, it is set at 10^{-8}. To guarantee convergence, the error in the average temperature on the endwall between two iterations should be less than 10^{-4}.

4. Results and Discussions

Figure 5 compares the endwall η contours for different patterns at S = 1% and F = 2%. The real gas model is chosen to deal with gas thermophysical properties. From the figure, coolant flow from endwall cooling holes interacts with coolant flows from the upstream slot, and a large coolant coverage region is found in the flow passage between two vanes. The arrangement of cooling holes on the endwall also affects the flow path of the passage vortex. In Pattern B and Pattern E, the shedding coolant flows develop along the mainstream and are easier to impinge on the SS of the vane. For different designs, the coolant coverage in the "tough" region is different, Pattern B, Pattern D, Pattern E, and Pattern F have better coolant coverage in the pressure-vane junction regions. The coolants have difficulty being ejected out from the LE regions of Pattern A, Pattern C, and Pattern D.

Considering gas thermophysical properties, comparisons of endwall η contours for different patterns are shown in Figure 6. Three kinds of gas thermophysical models are applied, respectively, the real gas model, ideal gas model, and constant property gas model. Pattern A and Pattern D, which are, respectively, based on pressure coefficient distributions and limiting streamline distributions, are used for comparisons. From the figure, the coolant injection is obviously strengthened in the case of constant property gas. It is indicated that the case of constant property gas has smaller coolant coverage in the wake region compared with the other cases. For the cases of real gas and ideal gas, there is larger coolant coverage in the wake region of the cooling holes. The cases of real gas and ideal gas have larger gas density at high temperature. To ensure the same mass flow rate, a smaller coolant injection velocity is obtained for the cases of real gas and ideal gas. However, the difference between the case with the real gas model and the case with the ideal gas model is very small because the temperature and pressure is far from the critical point.

Figure 7 compares the lateral averaged η of Pattern A and Pattern D with different gas thermophysical properties. From the figure, larger averaged η is found in the slot region for the case with constant property gas. This trend is totally different from the coolant coverage of the cooling holes for the case with constant property gas. The injection angle of 45° is for the shedding flow of the slot, while the injection angle of 30° is for the shedding flow of the cooling holes. For the coolant with the injection angle of 30°, the gas density is more dominant in determining coolant coverage, and the regions of the cooling holes for the cases with real gas and ideal gas have larger coolant coverage. However, for the injection angle of 45°, i.e., the slot region, the ejecting velocity is more dominant in determining coolant coverage, and the case with constant property gas has larger coolant coverage. In the region of $0 < x/C < 0.3$, the cases with the real gas model and ideal gas model have large coolant coverage. With the mixed flow developing on the endwall, the difference in coolant coverage for different cases becomes smaller, and they overlap together.

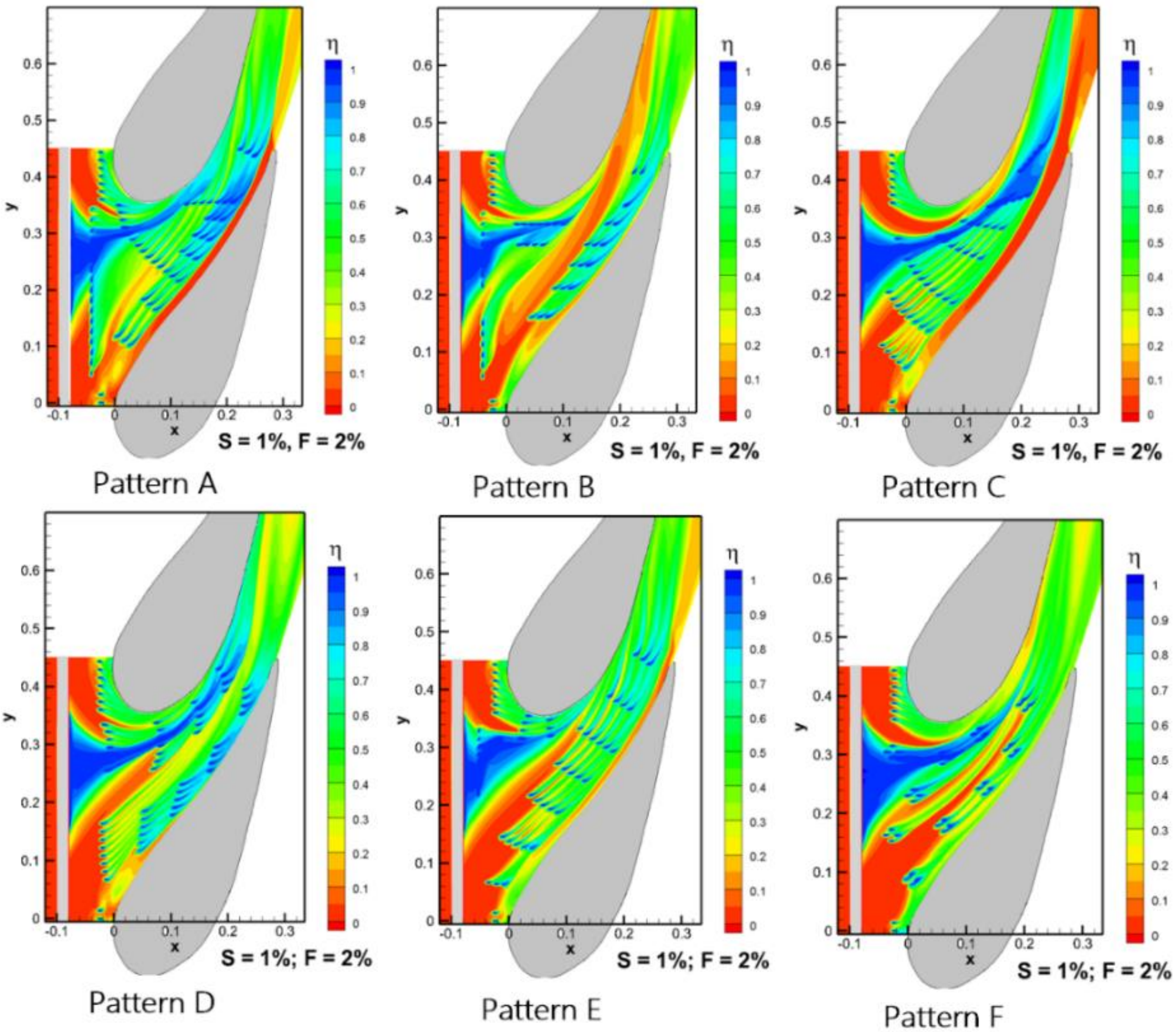

Figure 5. Endwall η contours for different patterns at S = 1% and F = 2% using the real gas model.

Figure 8 compares the endwall η contours for Pattern D at different cooling hole mass flow ratios with different gas thermophysical properties, i.e., the real gas model and constant property gas model. The mainstream temperature is set at 1700 K. The S is set at 1%, and F ranges from 1–2% in the considered cases. Overall, the coolant coverage is increased with the increased S, and a relatively full coolant coverage is found at F = 2%. However, the distributions of the coolant flow are totally different when different gas thermophysical models are applied, though the same coolant supply is set for all the cases. When F is set at 1% in the case of real gas, the coolant cannot eject from the cooling holes at the region around $x/C = 0$. For the case of constant property gas, the coolant coverage is obviously improved. At the temperature of 1700 K, the model of real gas has a larger density than the case of the constant property gas. The gas with smaller density has larger ejecting velocity, and is easily ejected from the upstream region. When the coolant supply is increased from F = 1.5% to 2%, the coolant is not increased obviously. It is expected that more coolant flows mix with the mainstream, and there is little coolant coverage on the endwall when the coolant with smaller density is applied. When a single cooling hole is obverted, an obvious cooling wake for the cooling holes in the case of the real gas model can be found. The increased F has a more obvious effect in the case with the real gas model. It is indicated that the gas with larger density can protect the wall better when the coolant ejecting velocity is increased. The coolant coverage from the upstream slot is almost the same for all the cases, which indicates that the coolant flows from the downstream cooling holes have no obvious effects on the coolant ejecting from the slot.

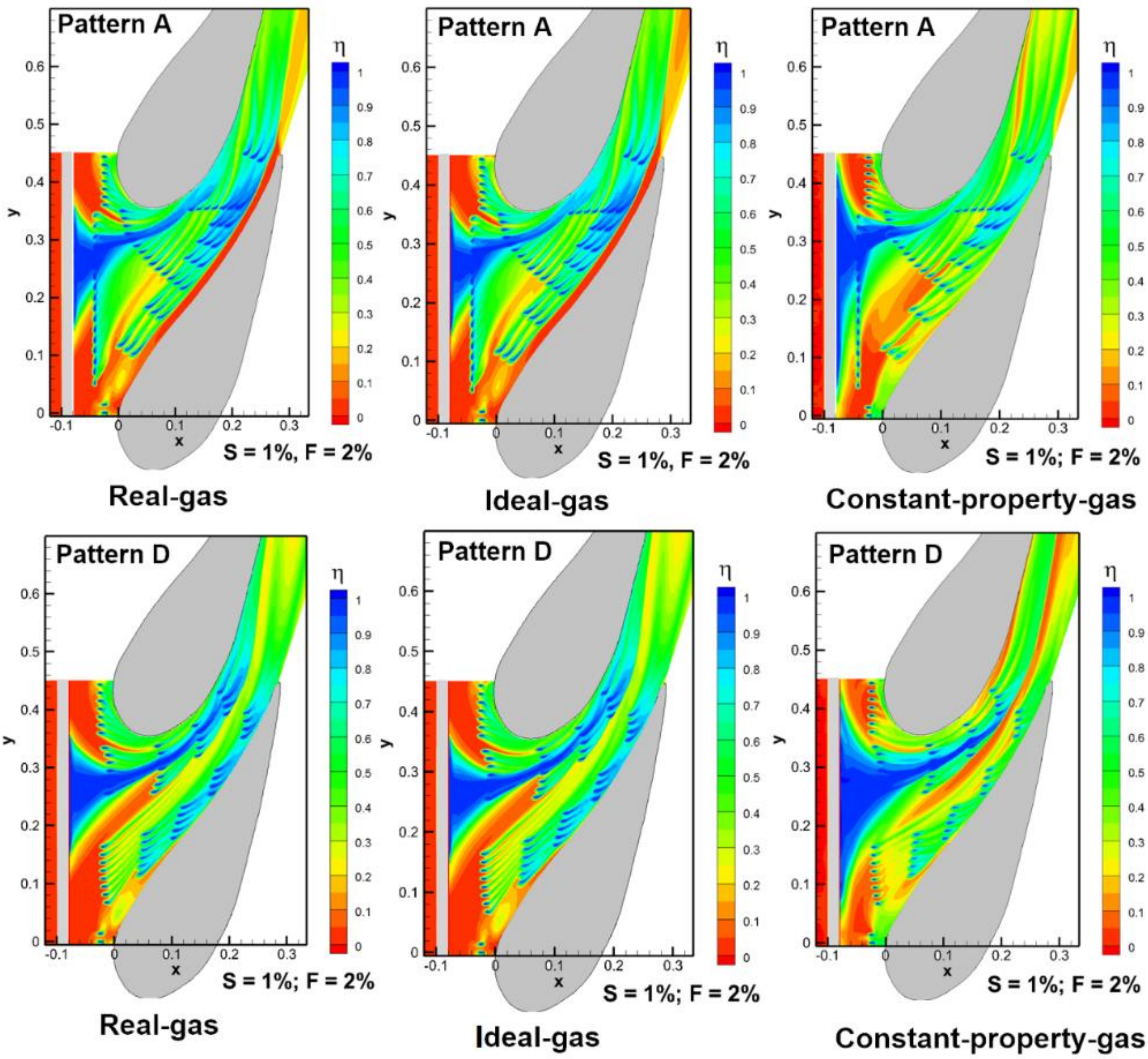

Figure 6. Comparisons of endwall η contours for Pattern A and Pattern D with different gas thermo-physical properties.

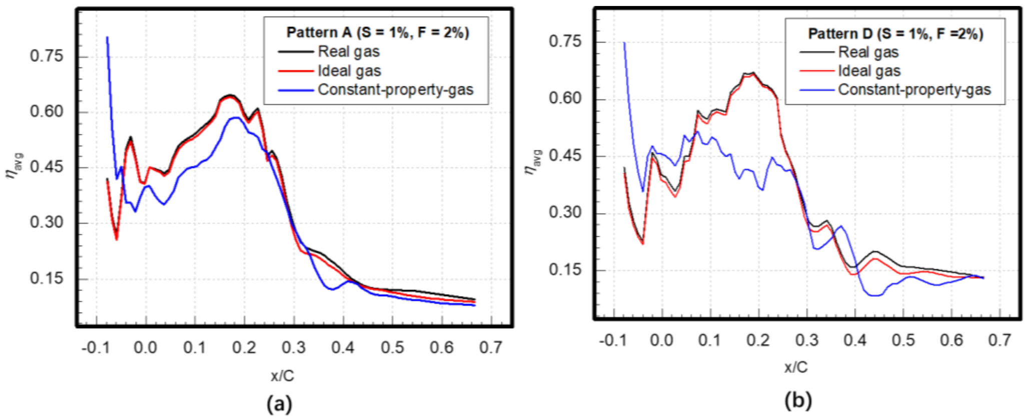

Figure 7. Comparisons of lateral averaged η for Pattern A and Pattern D at different gas thermophysical properties. (**a**) Pattern A; (**b**) Pattern D.

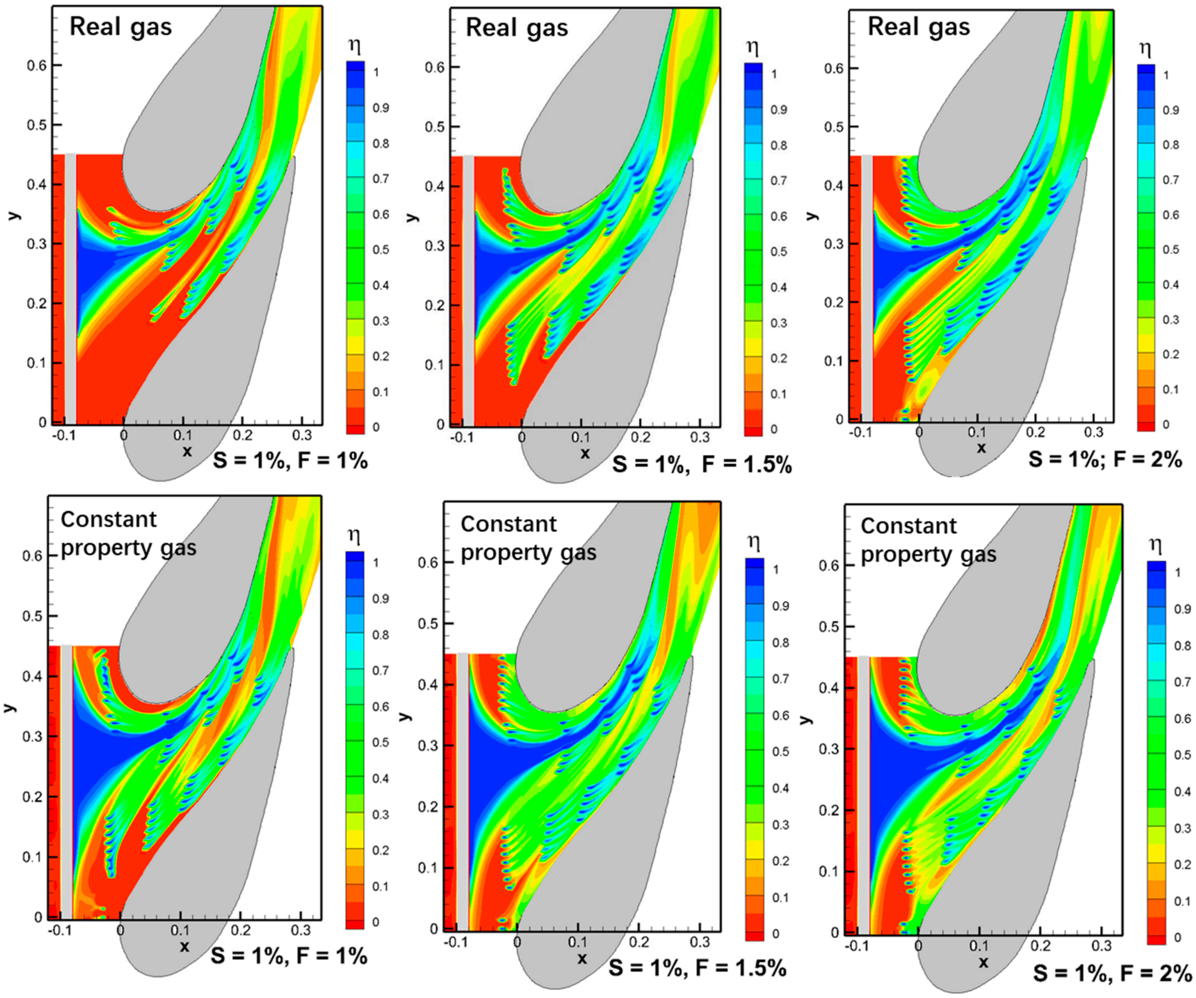

Figure 8. Comparisons of endwall η contours for Pattern D with different gas thermophysical properties at different cooling hole mass flow ratios.

Comparisons of lateral averaged η for Pattern D with different gas thermophysical properties at different cooling hole mass flow ratios are presented in Figure 9. From the figure, the distribution displays a trend of an increase at first, and then a decrease. The larger averaged η is found in the region of $0.1 < x/C < 0.3$, when large quantities of cooling holes are arranged. For the case with the real gas model, averaged η is increased with the increased F. However, the increased trend is weakened when the F is increased from 1.5%

to 2%. In addition, the distribution of averaged η is overlapped when the S is increased for the case with the constant property gas model. This phenomenon is caused by the different gas densities for different gas models at 1700 K. It is expected that the gas with larger density has the advantage of enlarging coolant coverage with the increased F.

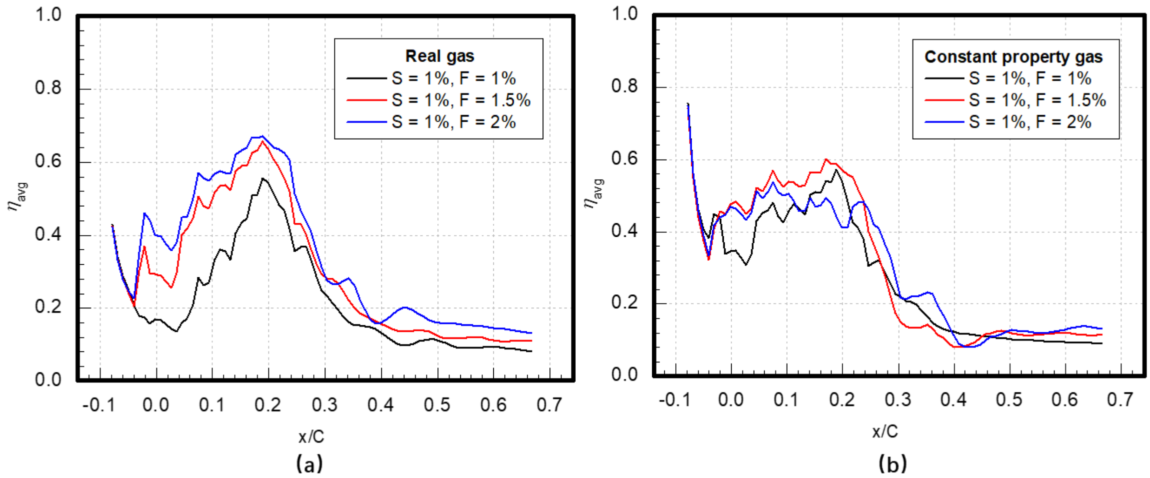

Figure 9. Comparisons of lateral averaged η distributions for Pattern D with different gas thermophysical properties at different cooling hole mass flow ratios. (**a**) For real gas; (**b**) For constant property gas.

Figure 10 compares endwall η contours for Pattern D with different gas thermophysical properties at different slot mass flow ratios. The S ranges from 1–2%, and the F is set as 2%. The mainstream temperature is also set at 1700 K. From the figure, it is clear that the ejected flows from the upstream slot have significant coolant coverage in the middle passage between two vanes. With the increased S, the coolant coverage is enlarged from the middle passage to the LE endwall and develops along the horseshoe vortex in the passage. The enlarged coolant coverage is more evident in the cases with the constant property gas model. However, the increase of coolant coverage is weakened in the case with the real gas model when S is increased from 1.5% to 2%. Similar to the phenomenon in Figure 8, the waking region is more obvious in the cases with the real gas model. For the case with the constant property gas model at the largest S, i.e., S = 2%, a relatively large and strong wake region is also found. It is indicated that when the ejected flows from the slot are very strong at a high velocity, it can change the pressure field of the downstream endwall. Because of the low-pressure field downstream of the shedding flows, it is beneficial for coolant coverage on the endwall.

Comparisons of lateral averaged η for Pattern D with different gas thermophysical properties at different slot mass flow ratios are displayed in Figure 11. Comparing Figures 9 and 11, it is found that the coolant flows from the slot mainly take effect in the region of $-0.1 < x/C < 0.1$, and slightly increased lateral averaged η is found in the region of $0.1 < x/C < 0.3$. In the region of $0.3 < x/C < 0.6$, the distribution trend is different in the cases with the real gas model, which proves the effect of the ejected flows from the slot on the downstream flow field. As expected, the increase of lateral averaged η is not obvious when the S is increased from 1.5% to 2%. However, the η in the cases of constant property gas is gradually improved when the S is increased from 1.0% to 2%. It is indicated that the increased velocity is more effective to improve the coolant coverage for the slot with an injection angle of 45°.

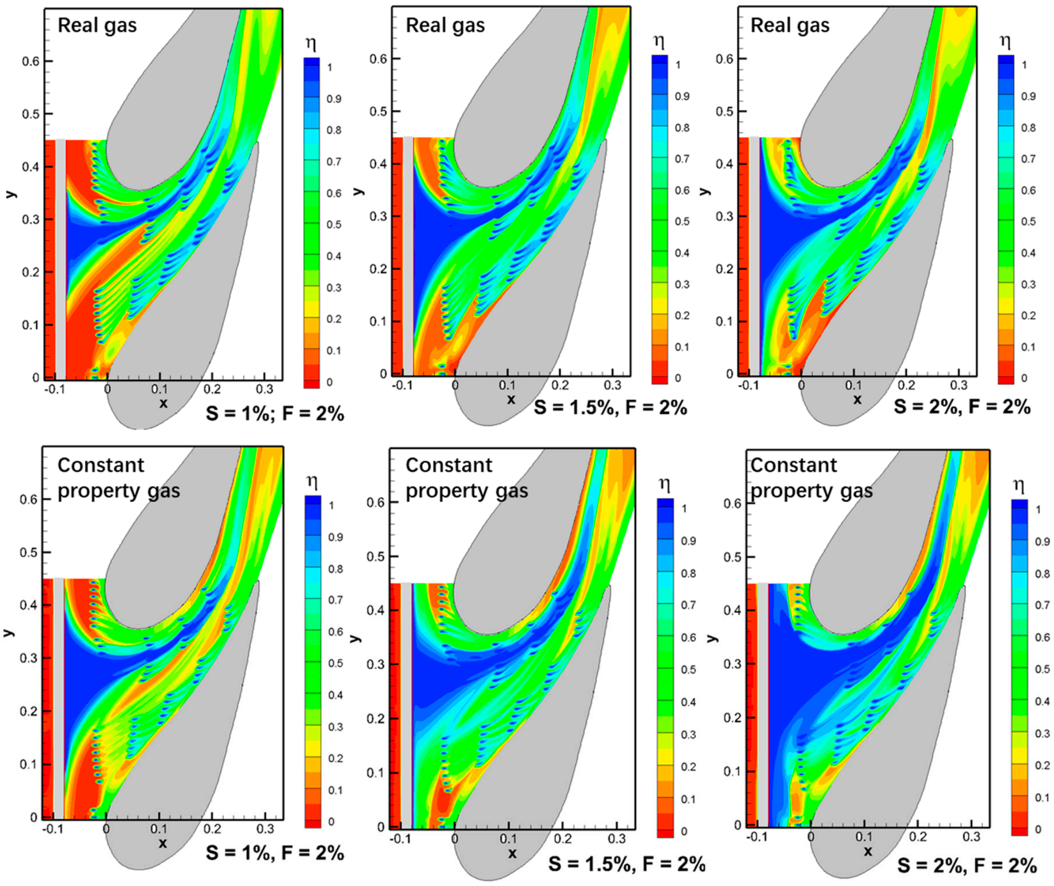

Figure 10. Comparisons of endwall η contours for Pattern D with different gas thermophysical properties at different slot mass flow ratios.

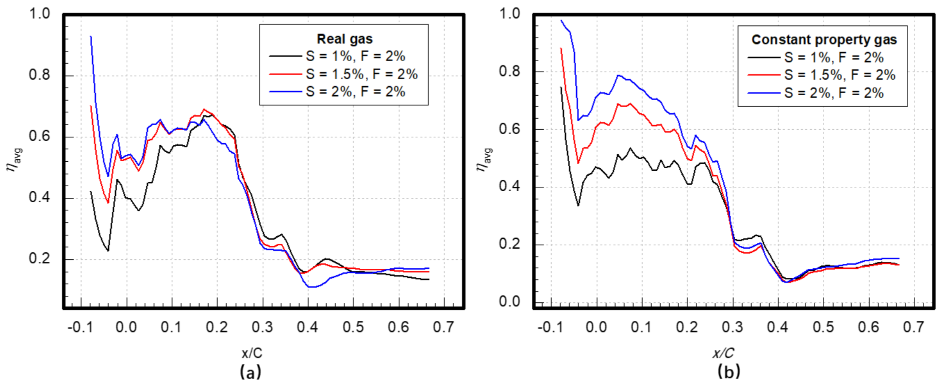

Figure 11. Comparisons of lateral averaged η for Pattern D with different gas thermophysical properties at different slot mass flow ratios. (**a**) For real gas; (**b**) For constant property gas.

Figure 12 compares endwall η contours for Pattern D with different gas thermophysical properties at different mainstream temperatures. The mainstream temperature ranges from 1700 K to 1100 K, with the same turbulence intensity. For the constant property gas model, the thermophysical property is obtained at the mainstream temperature, which can be found in Table 3. For the cases with the real gas model, the η distribution is changed when the mainstream temperature is changed. From the figure, it is found that the η from the upstream slot is enlarged with the decreased mainstream temperature from 1700 K to 1100 K. When the mainstream temperature is decreased, the density difference between the hot gas and the coolant flow becomes small and the mainstream velocity decreases. When the mainstream velocity is decreased, the coolant ejecting from the slot becomes easy and has benefits for coolant flows covering the endwall. It is expected that when the mainstream temperature is decreased to 700 K, the η contours become similar to the cases with the constant property gas. For the cases with constant property gas, the η contours almost stay the same when the mainstream temperature is changed. In addition, the wake region is more obvious in the cases with the real gas model, and it is gradually weakened when the mainstream temperature decreases from 1700 K to 1100 K. This also provides additional evidence that the determination of the coolant coverage of the slot and the cooling holes are different, i.e., the coolant coverage of the slot is more sensitive to the ejecting velocity of the slot and the coolant coverage of the cooling holes is more sensitive to the gas density.

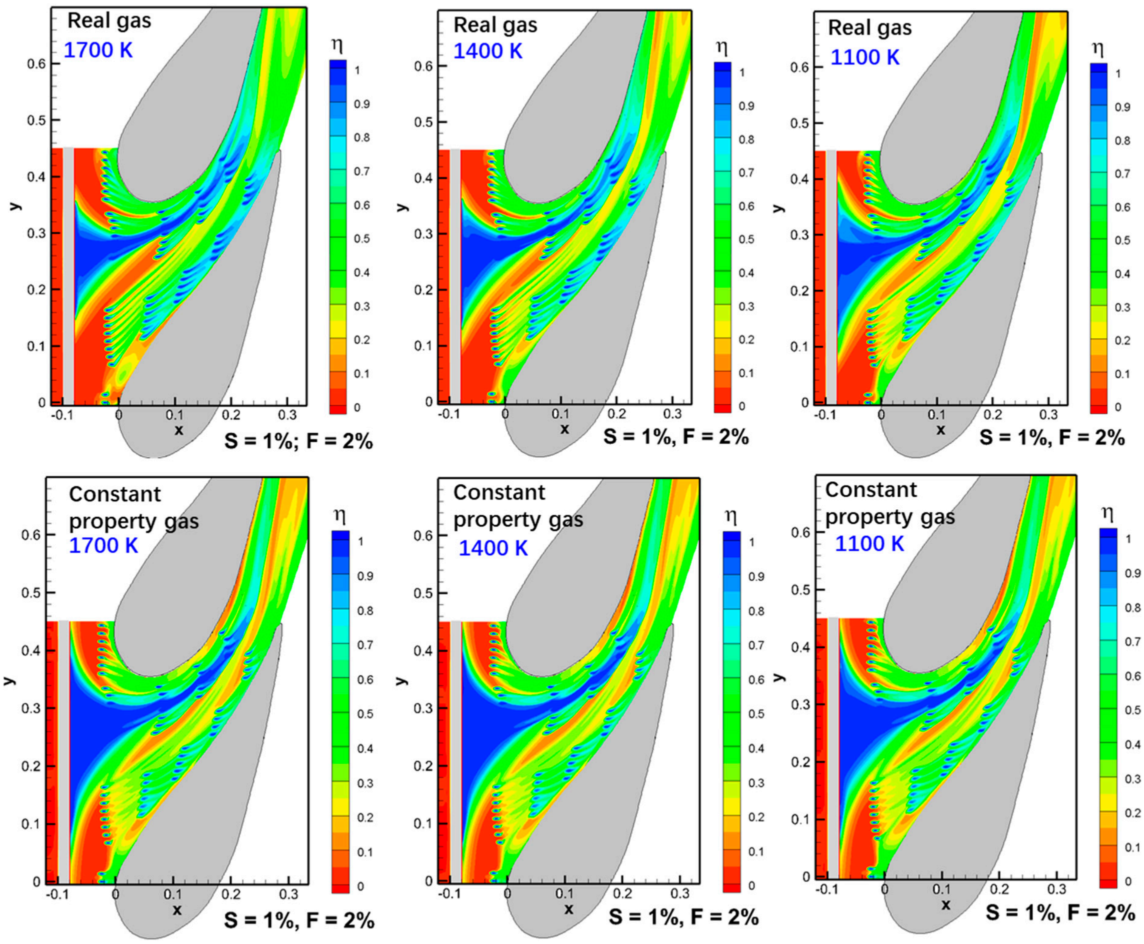

Figure 12. Comparisons of endwall η contours for Pattern D with different gas thermophysical properties at different mainstream temperatures.

Comparisons of lateral averaged η for Pattern D with different gas thermophysical properties at different mainstream temperatures are presented in Figure 13. As shown in the figure, the lateral averaged endwall η is increased with the decreased mainstream temperature in the region of $-0.1 < x/C < 0.1$, where the coolant flows from the slot mainly take effect. While in the region of $0.1 < x/C < 0.3$, the distribution of lateral averaged η is totally different when the mainstream temperature is decreased. For the cases with constant property gas, the distribution of lateral averaged η is almost the same. Therefore, it is concluded that the endwall η distribution is mainly determined by the relative ratio of ejecting velocity and density magnitude of the hot gas and the coolant. The effect of ejecting velocity and density magnitude on the coolant coverage differs at different ejecting angles, such as the slot and the cooling holes.

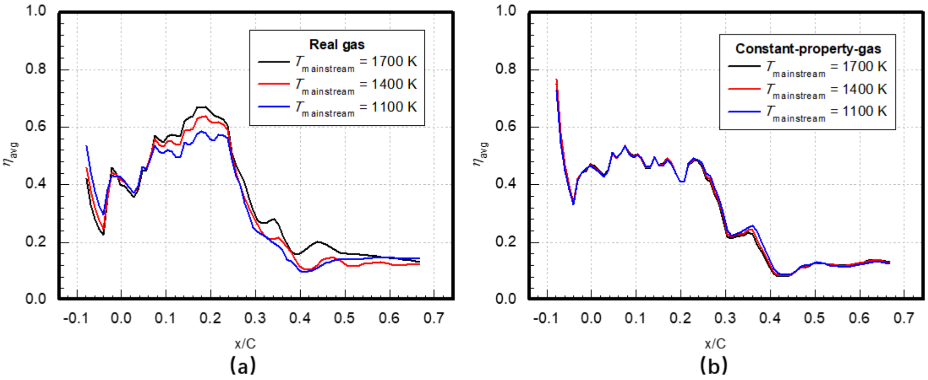

Figure 13. Comparisons of lateral averaged η for Pattern D with different gas thermophysical properties at different mainstream temperatures. (**a**) For real gas; (**b**) For constant property gas.

Three-dimensional streamlines and velocity distributions originating from slot and cooling holes for different patterns are shown in Figure 14. The mainstream is set at 1700 K, and the real gas model is applied for all the cases. The coolant injection from the slot interacts with the mainstream, and the mixing flows are drawn to the SS by the transverse pressure gradient. The coolant flows from the slot are hard to attach on the endwall when it develops along the flow passage. For the coolant from the endwall film cooling holes, it is accelerated along the flow passage, and pushed to the SS by the transverse pressure gradient. However, for different cases, the coolant coverage on the vane-PS junction region is different. From the figure, Patten B, Pattern D, and Pattern F have better coolant coverage in the "tough" region.

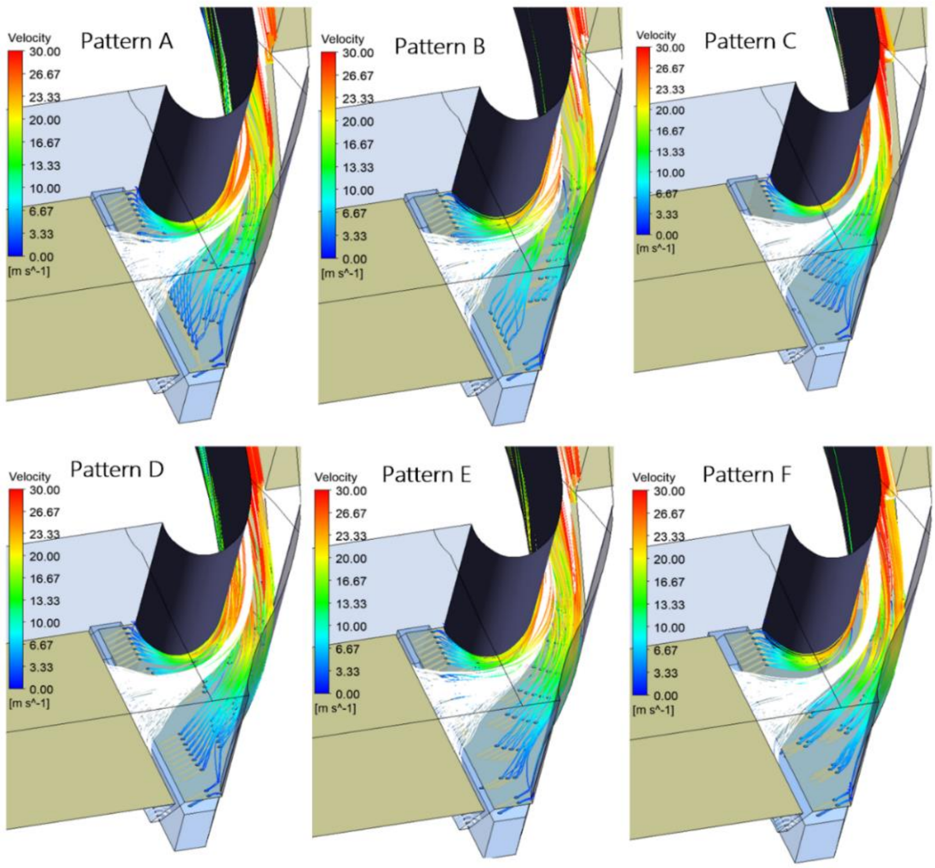

Figure 14. 3D streamlines and velocity distributions originating from slot and cooling holes for different patterns using real gas model.

Three-dimensional streamlines and velocity distributions originating from the slot and the cooling holes with different gas thermophysical properties are shown in Figure 15. It is clear that the coolant ejecting velocity is larger for the case with constant property gas in the figure. In addition, the coolant ejection from the slot is stronger than other cases, and the ejection region is enlarged. The larger ejection velocity has the benefit for coolant coverage in the region of the vane-PS junction. The difference between the cases of real gas and ideal gas is very small because the state of temperature and pressure is far from the critical point.

Figure 16 presents the streamlines originating from endwall film cooling holes interacting with the mainstream. The coolant flow developing along the vane passage is accelerated by the mainstream. It is also observed that a corner vortex is found in the region of the vane-PS junction region, which prevents the coolant from attaching on the endwall. From the PS to the SS, the transverse flow is accelerated and the velocity peak value is found on the suction side. The coolant ejection from the cooling holes in the LE region develops along the PS and is drawn upward by the mainstream. Therefore, the poor coolant coverage in the corner region exists.

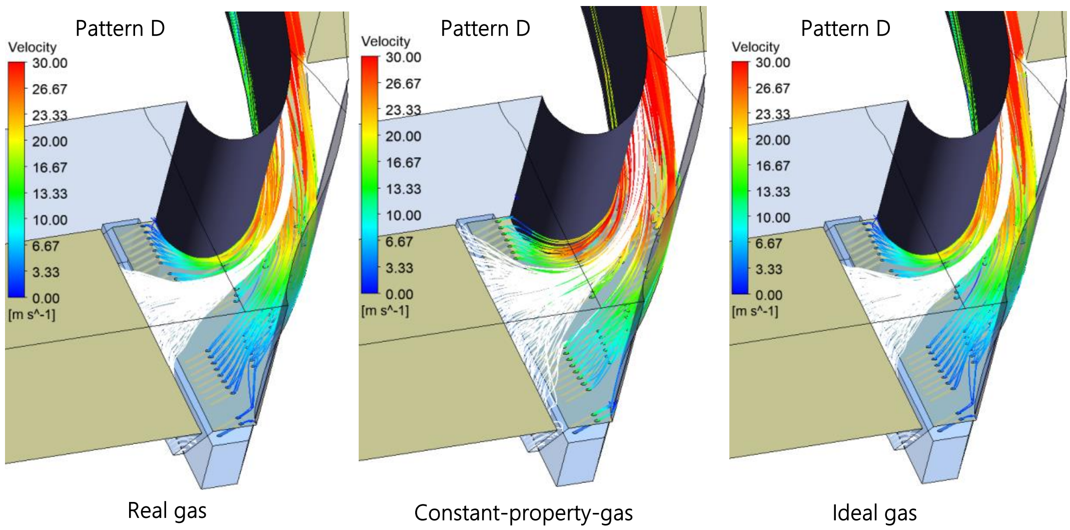

Figure 15. 3D streamlines and velocity distributions originating from the slot and the cooling holes with different gas thermophysical properties.

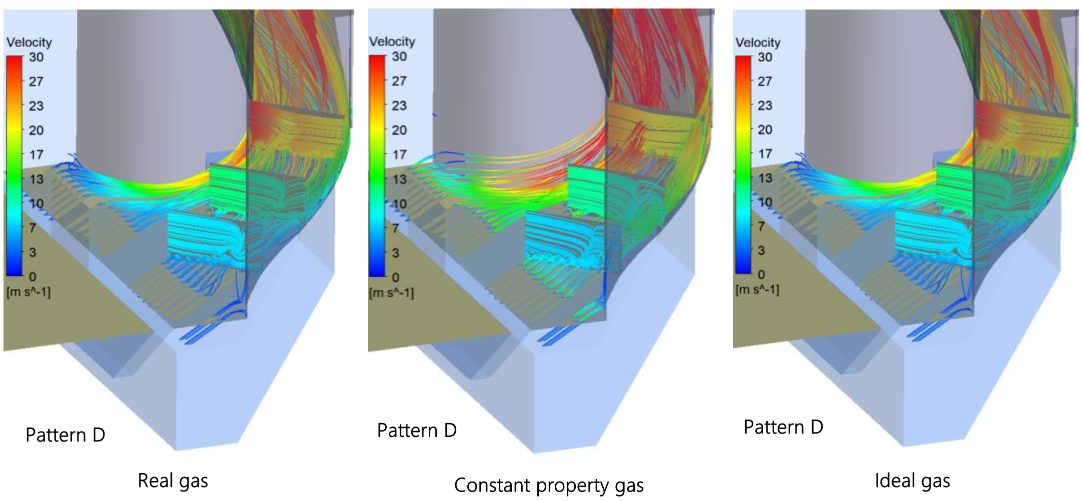

Figure 16. Interaction of 3D streamlines with mainstream flow for Pattern D with different gas thermophysical properties.

5. Conclusions

In the present study, the effects of gas thermophysical properties on full-range endwall film cooling are investigated at engine-like boundary conditions. Six kinds of full-range endwall film cooling designs are considered with the validated turbulence model, i.e., the k-ω SST model. Three kinds of gas thermophysical property models are considered, i.e., the real gas model, ideal gas model, and constant property gas model. Cooling efficiency and flow structures of full-range endwall film cooling are presented and discussed.

The coolant coverage in the PS-vane junction region is improved in Pattern B, Pattern D, Pattern E, and Pattern F with the application of the real gas model, which are designed based on the passage middle gap, limiting streamline, heat transfer coefficient, and the four-holes pattern. The coolants have difficulty being ejected out from the LE regions of Pattern A, Pattern C, and Pattern D because more cooling holes are arranged in the upstream regions.

The endwall η distribution is mainly determined by the relative ratio of ejecting velocity and density of the hot gas and the coolant. For the cases with the constant property gas model, i.e., the relative ratio of ejecting velocity and density is not changed, and the endwall η distribution almost has no changes, though different mainstream temperatures are applied. For the cases with the real gas model and the ideal gas model, they have larger gas density for the coolant flows from the cooling holes. For the case with the constant property gas, it has a larger ejecting velocity for the coolant flows from the slot. The effects of ejecting velocity and density magnitude on the coolant coverage differ at different ejecting angles. With an injection angle of 30°, the gas density is more dominant in determining the coolant coverage in the region of the cooling holes. At the injection angle of 45°, i.e., the slot region, the ejecting velocity is more dominant in determining the coolant coverage. Related conclusions provide good references for conducting endwall film cooling experiments in a room-temperature test rig, which ignores the effects of gas thermophysical properties.

Author Contributions: Conceptualization, J.L.; writing—original draft preparation, J.L. and M.X.; writing—review and editing, W.X.; All authors have read and agreed to the published version of the manuscript.

Funding: This work was supported by the Key Laboratory Continuously Supporting Project (grant No. WDZC6142703202216), the Natural Science Foundation of Hunan Province (Grant No. 2023JJ40733), and the National Natural Science Foundation of China (Grant No. 12272133).

Data Availability Statement: Not applicable.

Conflicts of Interest: The authors declare no conflict of interest.

Nomenclature

Latin characters

C	chord of the vane (m)
D	diameter of cooling holes (m)
F	cooling holes mass flow rate ratio
l	length of cooling holes (m)
P	pressure (pa)
P_c	pitch between two cooling holes (m)
P_v	pitch between adjacent vanes (m)
Re	Reynolds number
S	slot mass flow rate ratio
S_p	span of the vane (m)
T_g	mainstream temperature (K)
T_c	coolant temperature (K)
u	mainstream velocity (m/s)

x	streamwise direction (m)
y	spanwise direction (m)
z	normal direction (m)
Greek symbols	
α	injection angle (°)
λ	thermal conductivity (W/m·K)
η	film cooling effectiveness
μ	fluid dynamic viscosity (Pa·s)
ρ	fluid density (kg/m^3)
Subscripts	
m	average/overall
w	wall
c	coolant
Abbreviations	
HV	horseshoe vortex
LE	leading edge
PS	pressure side
SS	suction side
TI	turbulence intensity

References

1. Han, J.C.; Ekkad, S. Recent development in turbine blade film cooling. *Int. J. Rotating Mach.* **2001**, *7*, 21–40. [CrossRef]
2. Langston, L. Crossflows in a turbine cascade passage. *J. Eng. Gas Turbines Power* **1980**, *102*, 866–874. [CrossRef]
3. Friedrichs, S.; Hodson, H.; Dawes, W. Distribution of film-cooling effectiveness on a turbine endwall measured using the ammonia and diazo technique. ASME 1995 International Gas Turbine and Aeroengine Congress and Exposition. *J. Turbomach.* **1996**, *18*, V004T009A001.
4. Shi, W.; Chen, P.T.; Li, X.Y.; Ren, J.; Jiang, H.D. Uncertainty Quantification of the Effects of Small Manufacturing Deviations on Film Cooling: A Fan-Shaped Hole. *Aerospace* **2019**, *6*, 46. [CrossRef]
5. Oke, R.A.; Simon, T.W.; Burd, S.W.; Vahlberg, R. Measurements in a turbine cascade over a contoured endwall: Discrete hole injection of bleed flow. In *Turbo Expo 2000: Power for Land, Sea, and Air*; ASME: New York, NY, USA, 2000; p. V003T001A022.
6. Oke, R.; Simon, T.; Shih, T.; Zhu, B.; Lin, Y.L.; Chyu, M. Measurements over a film-cooled, contoured endwall with various coolant injection rates. In *Turbo Expo 2001: Power for Land, Sea, and Air*; ASME: New York, NY, USA, 2001; p. V003T001A025.
7. Zhang, L.J.; Jaiswal, R.S. Turbine Nozzle Endwall Film Cooling Study Using Pressure Sensitive Paint. In *Turbo Expo 2001: Power for Land, Sea, and Air*; ASME: New York, NY, USA, 2001; p. V003T001A030.
8. Knost, D.; Thole, K. Adiabatic effectiveness measurements of endwall film-cooling for a first stage vane. In *Turbo Expo 2004: Power for Land, Sea, and Air*; ASME: New York, NY, USA, 2004; pp. 353–362.
9. Ghosh, K.; Goldstein, R.J. Effect of inlet skew on heat/mass transfer from a simulated turbine blade. In Proceedings of the ASME 2011 Turbo Expo: Turbine Technical Conference and Exposition, Vancouver, BC, Canada, 6–10 June 2011; pp. 1677–1687.
10. Shiau, C.C.; Chen, A.F.; Han, J.C.; Azad, S.; Lee, C.P. Full-scale turbine vane endwall film-cooling effectiveness distribution using pressure-sensitive paint technique. *ASME J. Turbomach.* **2016**, *138*, 051002. [CrossRef]
11. Shiau, C.C.; Sahin, I.; Wang, N.; Han, J.C.; Xu, H.; Fox, M. Turbine Vane Endwall film cooling comparison from five film-hole design patterns and three upstream leakage injection angles. In *Turbo Expo 2018: Turbomachinery Technical Conference and Exposition*; ASME: New York, NY, USA, 2018; p. V05CT19A005.
12. Yang, X.; Liu, Z.; Zhao, Q.; Liu, Z.; Feng, Z.; Guo, F.; Ding, L.; Simon, T.W. Conjugate heat transfer measurements and predictions for the vane endwall of a high-pressure turbine with upstream purge flow. *Int. J. Heat Mass Transf.* **2019**, *140*, 634–647. [CrossRef]
13. Chen, P.; Wang, L.; Li, X.; Ren, J.; Jiang, H. Effect of axial turbine non-axisymmetric endwall contouring on film cooling at different locations. *Int. J. Heat Mass Transf.* **2020**, *147*, 118995. [CrossRef]
14. Chen, P.; Xue, Q.; Li, X.; Ren, J.; Jiang, H. Full coverage film cooling on a non-axisymmetric contoured endwall and the baseline endwall. *Int. J. Therm. Sci.* **2020**, *158*, 106562. [CrossRef]
15. Liu, J.; Du, W.; Hussain, S.; Xie, G.; Sundén, B. Endwall film cooling holes design upstream of the leading edge of a turbine vane. *Numer. Heat Transf. Part A Appl.* **2021**, *79*, 222–245. [CrossRef]
16. Bu, H.; Guo, Z.; Song, L.; Li, J. Effects of cooling configurations on the aerothermal performance of a turbine endwall with jet impingement and film cooling. *ASME J. Turbomach.* **2021**, *143*, 061013. [CrossRef]
17. Yang, X.; Zhao, Q.; Liu, Z.; Liu, Z.; Feng, Z. Film cooling patterns over an aircraft engine turbine endwall with slot leakage and discrete hole injection. *Int. J. Heat Mass Transf.* **2021**, *165*, 120565. [CrossRef]
18. Yan, D.J.; Jiang, H.M.; Li, J.L.; Xie, W.B.; Wang, Z.G.; Lu, S.P.; Zhang, Q. Influence of gas-to-wall temperature ratio on the leakage flow and cooling performance of a turbine squealer tip. *Aerospace* **2022**, *9*, 627. [CrossRef]
19. Knost, D.G.; Thole, K.A. Computational predictions of endwall film-cooling for a first stage vane. In *Turbo Expo 2003*; ASME: New York, NY, USA, 2003; pp. 163–173.

20. Knost, D.G. Predictions and Measurements of Film-Cooling on the Endwall of a First Stage Vane. Ph.D. Thesis, Virginia Tech, Blacksburg, VA, USA, 2003.
21. Liu, J.; Du, W.; Zhang, G.; Hussain, S.; Wang, L.; Xie, G.; Sundén, B. Design of Full-Scale Endwall Film Cooling of a Turbine Vane. *ASME J. Heat Transf.* **2020**, *142*, 022201. [CrossRef]
22. Pu, J.; Zhang, T.; Wang, J. Experimental study of cooling air effect on overall cooling of laminated configuration at a turbine vane end-wall. *Case Stud. Therm. Eng.* **2022**, *32*, 101890. [CrossRef]
23. Zhang, H.W.; He, Y.L.; Tao, W.Q. Numerical study on liquid-film cooling at high pressure. *Numer. Heat Tranfer Part A Appl.* **2010**, *58*, 163–186. [CrossRef]
24. Nematollahi, O.; Nili-Ahmadabadi, M.; Kim, K.C. The influence of cubic real-gas equations of state in the supersonic regime of dense gases. *J. Mech. Sci. Technol.* **2020**, *34*, 1581–1589. [CrossRef]
25. Yuan, F.; Zeng, Y.; Khoo, B.C. A new real-gas model to characterize and predict gas leakage for high-pressure gas pipeline. *J. Loss Prev. Process Ind.* **2022**, *74*, 104650. [CrossRef]
26. Salvadori, S.; Ottanelli, L.; Jonsson, M.; Ott, P.; Martelli, F. Investigation of High-Pressure Turbine Endwall Film-Cooling Performance Under Realistic Inlet Conditions. *J. Propuls. Power* **2012**, *28*, 799–810. [CrossRef]
27. Wen, F.B.; Hou, R.; Luo, Y.X.; Wang, S.T. Study on leading-edge trenched holes arrangement under real turbine flow conditions. *Eng. Appl. Comput. Fluid Mech.* **2021**, *15*, 781–797. [CrossRef]
28. Deng, Q.H.; Wang, H.H.; He, W.; Feng, Z.P. Cooling Characteristic of a Wall Jet for Suppressing Crossflow Effect under Conjugate Heat Transfer Condition. *Aerospace* **2022**, *9*, 29. [CrossRef]
29. Bai, B.; Li, Z.G.; Li, J.; Mao, S.; Ng, W.F. The Effects of axisymmetric convergent contouring and blowing ratio on endwall film cooling and vane pressure side surface phantom cooling performance. *ASME J. Eng. Gas Turbines Power* **2022**, *144*, 021020. [CrossRef]
30. Florio, L.A. Effect of gas equation of state on CFD predictions for ignition characteristics of hydrogen escaping from a tank. *Int. J. Hydrog. Energy* **2014**, *39*, 18451–18471. [CrossRef]
31. Song, W.H.; Yao, J.; Ma, J.S.; Li, Y.; Han, W.C. A pore structure based real gas transport model to determine gas permeability in nanoporous shale. *Int. J. Heat Mass Transf.* **2018**, *126*, 151–160. [CrossRef]
32. Nicklas, M. Film-cooled turbine endwall in a transonic flow field: Part ii—Heat transfer and film-cooling effectiveness. *ASME J. Turbomach.* **2001**, *123*, 720–729. [CrossRef]
33. Kang, M.B.; Kohli, A.; Thole, K. Heat transfer and flowfield measurements in the leading edge region of a stator vane endwall. *ASME J. Turbomach.* **1999**, *121*, 558–568. [CrossRef]
34. Poling, B.E.; Prausnitz, J.M.; O'connell, J.P. *Properties of Gases and Liquids*; McGraw-Hill Education: New York, NY, USA, 2001.